Investigation of Interstitials in Electron-Irradiated Aluminum by Diffuse-X-Ray Scattering Experiments

P. Ehrhart and W. Schilling*
Institut für Festkörperforschung der Kernforschungsanlage Jülich, Jülich, Germany
(Received 26 February 1973)

The diffuse scattering of x rays (Cu $K_{\alpha 1}$) from single crystals of aluminum has been investigated after low-temperature electron irradiation (defect concentrations 3×10^{-4} and 5×10^{-4}). The measurements were made near the (200), (400), (220), and (222) Bragg reflections in directions both parallel and perpendicular to the scattering vector. These measurements were repeated after a number of steps in an isochronal-recovery program. The data taken immediately after the irradiation showed all the characteristic features predicted by the theory for scattering from point defects with weak displacement fields (Huang scattering). The conclusions are the following: (i) The interstitial in Al has slightly tetragonal or cubic symmetry; the crowdion configuration can be excluded. (ii) By comparing the diffuse-scattering intensities with measurements of the lattice parameter the absolute defect concentration and the volume change ΔV per defect was determined. ($\Delta V = 1.9 \pm 0.2$ atomic volumes per Frenkel defect.) From the absolute concentration and from electrical-resistivity change measurement on the same sample, the resistivity change was determined to be $\rho_F = 3.9 \pm 0.6$ $\mu\Omega$ cm per atomic percent Frenkel defects. In the recovery measurements an increase of the scattering intensity per defect was observed at the end of stage I. This gives direct evidence that the interstitials agglomerate during their free migration in stage I. In stage II a further increase of the scattering intensity per interstitial is observed close to the Bragg peaks, suggesting an increase of the average interstitial cluster size throughout this stage. The changes in the intensity distribution around the reflections were in good agreement with the predictions of the scattering theory for defects with strong displacement fields (Stokes-Wilson approximation). From the data, the mean number of interstitials per cluster can be estimated. It is 2 at the end of stage I and increases to about 10 at the beginning of stage III. There is good indication that the larger interstitial clusters are dislocation loops.

I. INTRODUCTION

Irradiation of crystals at low temperatures produces vacancies and interstitials in equal numbers. In a fcc lattice, symmetry considerations suggest six possible configurations for an interstitial: the octahedral O, tetrahedral T, crowdion C, and three dumbbell configurations H_O, H_C, and H_T with the axis along the ⟨100⟩, ⟨110⟩ and ⟨111⟩ directions, respectively. Which configuration the interstitial takes in reality is not known. From model calculations for copper, it has been concluded that the dumbbell H_O should be the most stable configuration.[1-3] But with small changes in the interatomic potentials, other configurations may also be energetically more favorable.[4] There are no direct experimental results which clearly allow the discrimination between the various configurations. Most of the investigations of radiation damage in metals have been done with experimental techniques that do not react specifically to the detailed properties of the interstitials and vacancies, e.g., electrical resistivity, volume expansion, and stored energy. On the other hand, the question of the structure of the interstitial is of great importance for a better understanding of radiation damage, especially for the clarification of the defect reactions which occur during annealing. We restrict our consideration to two widely discussed recovery models: the conversion-two-interstitial[5,6] and the one-interstitial models.[6,7] The first model predicts that the interstitial is produced in the crowdion configuration C during low-temperature irradiation. This configuration is assumed to be metastable so that crowdions can convert at higher temperatures to a stable interstitial configuration (presumed H_O). In this model both recovery in stage I and in stage III are interpreted as free-interstitial migration. The one-interstitial model assumes that the interstitials are produced in their stable configuration. Therefore only stage I can be explained by interstitial migration, whereas stage III is attributed to vacancy migration.

Experimental methods that can give information about the structure of the interstitial are mechanical-relaxation experiments[8] (Snoek effect), anomalous transmission of x rays (Borrmann effect),[9] and the diffuse scattering of x rays and neutrons.[10,11] The diffuse scattering seems to be the most powerful method for the determination of the structure of point defects in crystals. It allows the measurement of the symmetry and the strength of the defects in a straightforward manner and is also a very sensitive method for observing defect clustering. Although the theory of the diffuse scattering by defects with displacement fields has been known for more than 25 years,[12,13] the experimental difficulties associated with low intensities and high background (i.e., thermal dif-

fuse scattering and Compton scattering) made diffuse-scattering measurements at statistically distributed point defects possible only very recently.[14,15] The technique of diffuse scattering has first been used for investigations on systems which give higher scattering intensities such as high-concentration solid solutions and defect clusters with strong displacement fields. The most detailed x-ray investigations on defect clusters are those on neutron-irradiated copper[16,17] and those of LiF after room-temperature γ irradiation [18,19]

For statistically distributed point defects with weak displacement fields, the diffuse-scattering cross section is essentially given by the Fourier transform of the displacement field around a single defect. According to the properties of the Fourier transformation, the displacements in the immediate neighborhood of the defect govern the scattering intensity near the Brillouin-zone boundary whereas the $1/R^2$ displacement field at large distances R from the defect dominates the scattering near the Bragg peaks. Near the peaks a strong increase in diffuse intensity is observed (Huang scattering), while the intensity in the Brillouin zone is normally very weak.

The present work describes an apparatus for measuring the Huang scattering for defect concentrations of $\sim 10^{-4}$. Measurements were performed on aluminum after low-temperature electron irradiation. From these measurements we obtain the symmetry and strength of the long-range displacement field of the interstitials. Huang-scattering measurements after different annealing treatments yield information about clustering reactions of interstitials at higher temperatures.

II. THEORY

The theory of diffuse scattering from point defects and defect clusters has recently been reviewed by Dederichs.[11] In the following we summarize only those parts which are necessary for the interpretation of our Al data following closely the notation introduced in Ref. 11. Additional theoretical treatments of diffuse scattering from defects have been published.[20–22]

Assuming a statistical distribution of defects, low defect densities, and linear superposition of the strain fields around the defects, one obtains for the diffuse scattering cross section per atom

$$S_{diff} = C\,|F(\vec{k})|^2 \tag{1a}$$

with

$$F(\vec{k}) = f^D_{\vec{k}} + f_{\vec{k}} \sum_n e^{i\vec{k}\cdot\vec{R}^n}(e^{i\vec{k}\cdot\vec{t}^n} - 1)$$

$$= f^D_{\vec{k}} + f_{\vec{k}} \sum_n e^{i\vec{q}\cdot\vec{R}^n}(e^{i\vec{k}\cdot\vec{t}^n} - 1), \tag{1b}$$

where $\vec{k}$ is the scattering vector, $\vec{R}^n$ the position vector of atom number n in the "average" lattice, i.e., in a lattice homogeneously expanded by all the other defects in the crystal. $\vec{t}^n$ is the static displacement of atom n due to the defect. C is the defect concentration in atomic fractions, $\vec{q}$ the difference $\vec{k} - \vec{h}$ between $\vec{k}$ and the nearest reciprocal-lattice vector $\vec{h}$, and $f_{\vec{k}}$ is the atomic-scattering factor. (For simplicity, only one atom per unit cell is assumed.) The "defect-structure factor" $F(\vec{k})$ characterizes the scattering behavior of one defect. $F(\vec{k})$ is made up of two contributions: the scattering factor $f^D_{\vec{k}}$ of the defect itself and the contribution due to the displacement field $\vec{t}^n$ around the defect. For an atom at an interstitial position,

$$f^D_{\vec{k}} = f_{\vec{k}} e^{i\vec{k}\cdot\vec{R}^I}, \tag{2a}$$

and for a split interstitial,

$$f^D_{\vec{k}} = f_{\vec{k}}(\cos\vec{k}\cdot\vec{R}^I - 1). \tag{2b}$$

$\vec{R}^I$ denotes the position vector of the interstitial within the unit cell. For a vacancy, $f^D_{\vec{k}} = -f_{\vec{k}}$. The defect densities for which Eqs. (1) are a good approximation are determined[21] by the condition that

$$kt^{(1)} \ll 1, \tag{3}$$

where $t^{(1)}$ are the displacements resulting from one defect at a distance equal to the average separation $\langle l\rangle = (V_c/C)^{1/3}$ between defects (V_c = atomic volume).

A. Small-q Approximation for S_{diff}: Huang Scattering

If the vector $\vec{q}$ is small enough, the diffuse scattering images primarily the long-range part of the displacement field around the defect. In this case the exponential in parentheses in Eq. (1b) can be expanded and S_{diff} can be expressed in terms of the Fourier transform $\tilde{t}(\vec{q})$ of the displacement field as ($\vec{h} \simeq \vec{k}$),

$$S_{diff}(\vec{k}) = S_{Huang}(\vec{k}) + S_{anti}(\vec{k}), \tag{4a}$$

where the main term is

$$S_{Huang}(\vec{k}) = Cf^2_{\vec{h}}\,|\vec{h}\cdot\tilde{\vec{t}}(\vec{q})|^2 \tag{4b}$$

and

$$S_{anti}(\vec{k}) = 2Cf^2_{\vec{h}}\eta(\vec{h})[\vec{h}\cdot\tilde{\vec{t}}(\vec{q})] \tag{4c}$$

with

$$\eta(\vec{h}) = \sum_n (1 - \cos\vec{h}\cdot\vec{t}^n) - \mathrm{Re}(f^D_{\vec{h}}/f_{\vec{h}}). \tag{4d}$$

$S_{anti}(\vec{k})$ is antisymmetric with respect to the direction of $\vec{q}$ and will be discussed in Sec. II B. The symmetric term S_{Huang} can be found from the experimental data by averaging the intensities observed at equal distances but opposite directions from the Bragg peak. The exact condition for which Eqs. (4a)–(4d) are good approximations is

$qR_0 \ll 1$, where R_0 is that distance from the defect center at which the displacements are of the order of $2\pi/h$. For point defects, this condition is well fulfilled if only $q \ll h$; for defect clusters, the limitations are more serious (see Sec. II C).

For the further evaluation of $\vec{t}(\vec{q})$ entering in both S_{Huang} and S_{anti}, elastic-continuum theory is used. This is a good approximation for the case considered here, where most of the scattering comes from larger distances from the defect center. In this case it is convenient to imagine the defect being replaced by an arrangement of forces which—at larger distances—produce the same displacements as the defect. The first moment of this arrangement of forces defines the so-called dipole tensor P_{ij} of the defect, just as the first moment of the distribution of electrical charges (*scalars*) defines the electric-dipole *vector*. The symmetry of this dipole tensor reflects the angular symmetry of the long-range part of the displacement field, whereas the radial variation of the long-range displacement field is always like $1/R^2$. Expressing $\vec{t}(\vec{q})$ in terms of the components of the dipole tensor P_{ij} for cubic crystals, the following formula is obtained for the Huang scattering[11,21]:

$$S_{\text{Huang}}(\vec{k}) = Cf\tfrac{2}{h}(h/q)^2[\gamma^{(1)}\pi^{(1)} + \gamma^{(2)}\pi^{(2)} + \gamma^{(3)}\pi^{(3)}], \quad (5)$$

where $\gamma^{(1)}$, $\gamma^{(2)}$, and $\gamma^{(3)}$ are factors which depend on the elastic constants of the medium and on the directions of $\vec{q}$ and $\vec{h}$. General formulas for the calculation of $\gamma^{(1)}$, $\gamma^{(2)}$, and $\gamma^{(3)}$ as well as explicit expressions for high-symmetry directions are given in Ref. 21. (See also Table II for explicit values for Al.) $\pi^{(1)}$, $\pi^{(2)}$, and $\pi^{(3)}$ are quadratic expressions of the dipole force-tensor components:

$$\pi^{(1)} = \frac{1}{3}\left(\sum_i P_{ii}\right)^2, \quad (6a)$$

$$\pi^{(2)} = \frac{1}{6}\sum_{i>j}(P_{ii} - P_{jj})^2, \quad (6b)$$

$$\pi^{(3)} = \frac{2}{3}\sum_{i>j} P_{ij}^2. \quad (6c)$$

The quantity $\pi^{(1)}$ characterizes the strength of the defect. It also determines the lattice-parameter change as

$$\frac{\Delta a}{a} = C\,\frac{(\frac{1}{3}\pi^{(1)})^{1/2}}{V_c(C_{11}+2C_{12})}, \quad (7)$$

where C_{11} and C_{12} are elastic constants and V_c is the atomic volume. The quantities $\pi^{(2)}$ and $\pi^{(3)}$ characterize the deviation from cubic symmetry of the long-range displacement field (see Table I for details).

For the derivation of Eqs. (5)–(7) the assumption has been made that for defects with lower than cubic symmetry (for which $\pi^{(2)}$ and/or $\pi^{(3)} \neq 0$) their symmetry axes are distributed equally over all possible equivalent orientations in the crystal.

TABLE I. Parameters $\pi^{(2)}$ and $\pi^{(3)}$ for point defects of different symmetry and planes P and lines L of zero diffuse scattering around the reflections of type $(h00)$, $(hh0)$, and (hhh).

Defect symmetry and Symmetry axis	$\pi^{(2)}$	$\pi^{(3)}$	Reflection $(h00)$	$(hh0)$	(hhh)
Cubic	0	0	$P \perp [100]$	$P \perp [110]$	Surface $\perp [111]$
Tetragonal $\langle 100 \rangle$	+	0	$P \perp [100]$	$L \parallel [001]$	···
Trigonal $\langle 111 \rangle$	0	+	···	$L \parallel [110]$	···
Orthorhombic $\langle 110 \rangle$	+	+	···	···	···

From Eqs. (5)–(7) the following characteristic features can be recognized.

(i) The diffuse-scattering intensity is proportional to the defect concentration C. This is a consequence of the high dilution and statistical distribution of defects. The latter assumption is essential to guarantee cancellation of the interference terms arising from all the waves scattered at the different defects.

(ii) The Huang scattering is proportional to h^2/q^2. This reflects directly the $1/R^2$ dependence of the long-range displacement field. This $1/q^2$ dependence is responsible for the strong increase of S_{Huang} towards the Bragg peak.

(iii) The shape of the intensity distribution around the different reflections is determined both by the variation of the coefficients $\gamma^{(1)}$ to $\gamma^{(3)}$ in the brackets of Eq. (5) with the directions of $\vec{q}$ and $\vec{h}$ and by the magnitudes of the defect parameters $\pi^{(1)}$ to $\pi^{(3)}$. This dependence of the intensity distribution on the defect parameters $\pi^{(1)}$ to $\pi^{(3)}$ is one of the most important features of diffuse scattering which provides the possibility of discriminating between the different interstitial configurations mentioned in Sec. I.[21] As mentioned above, the expression in the brackets of Eq. (5) already contains an averaging process over all equivalent defect orientations. For defects which are all aligned (only one orientation), there would always exist a plane through the reciprocal-lattice point at which $\vec{t}(\vec{q})$, and therefore also S_{Huang}, would vanish. The position of this plane would uniquely determine the defect symmetry. By averaging over all equivalent orientations, the occurrence of such zero-intensity planes at all reflections, in general, gets lost. However, for some high-symmetry direction in $\vec{q}$ and $\vec{h}$ the zero-intensity planes may coincide or cross in a common line. These situations are summarized in Table I. Inspection of this table reveals that by looking for

zero-intensity lines (or planes), for instance in the [100] and [110] directions around an ($hh0$) reflection, a unique discrimination between cubic, tetragonal, trigonal, and orthorhombic defect symmetries is possible, even if the defect axes are distributed over all equivalent orientations. For Al in Table II the factors $\gamma^{(1)}$ to $\gamma^{(3)}$, entering into the expression in the brackets of Eq. (5), are summarized for different directions and reflections. From this table one recognizes again how by measuring the diffuse intensity in different $\vec{q}$ directions around different reflections the parameters $\pi^{(1)}$, $\pi^{(2)}$, and $\pi^{(3)}$ can be found.

(iv) If one takes $\mathrm{Tr}P_{ij} = (3\pi^{(1)})^{1/2}$ as a measure for the defect strength, according to Eqs. (5) and (7) the Huang intensity contains the combination $C(\mathrm{Tr}P_{ij})^2$, whereas the lattice-parameter change is proportional to $C(\mathrm{Tr}P_{ij})$. Therefore in a sample with an unknown defect density C, measurements of both S_{Huang} and of $\Delta a/a$ can determine the absolute value of C. This seems to be the only method by which absolute concentrations of Frenkel pairs can be obtained experimentally in irradiated samples.

For application to radiation damage it is further important to recognize that the defect strength of a vacancy is typically ten times smaller than for an interstitial. Therefore the interstitials completely dominate S_{diff} in irradiated samples.

Furthermore, the occurrence of $\pi^{(1)} \propto (\mathrm{Tr}P_{ij})^2$ in S_{Huang} makes diffuse scattering a very sensitive tool to detect interstitial clustering. If, for simplicity, we assume that the displacements of the interstitials making up a cluster superimpose linearly, then the components of the dipole force tensor of the cluster are just N times the tensor components of the single defects, where N is the number of interstitials per cluster. Since the concentration of clusters is C/N it follows that

$$S_{\mathrm{Huang}}^{\mathrm{cluster}} = (C/N)N^2 S_{\mathrm{Huang}}^{\mathrm{single\ interst.}} = CNS_{\mathrm{Huang}}^{\mathrm{single\ interst.}}. \quad (8)$$

Equation (8) says that, upon clustering, the contribution per interstitial to the Huang scattering increases linearly with the cluster size if the displacements are additive. If they are not exactly additive, one still expects an appreciable increase of the scattering intensity during cluster formation.

TABLE II. Parameters $\gamma^{(1)}$, $\gamma^{(2)}$, and $\gamma^{(3)}$ entering into Eq. (5) for some high-symmetry reflections and $\vec{q}$ directions. The parameters have been calculated according to the formulas given in Refs. 11 and 21 using the low-temperature elastic constants of Al (Ref. 40): $C_{11} = 1.143 \times 10^{12}$ dyn/cm^2, $C_{12}/C_{11} = 0.539$, $C_{44}/C_{11} = 0.276$. The γ parameters are given in units of $(3V_c^2 C_{11}^2)^{-1} = (425\ \mathrm{eV}^2)^{-1}$, V_c = atomic volume.

Type of reflection	Direction of $\vec{q}$	$\gamma^{(1)}$	$\gamma^{(2)}$	$\gamma^{(3)}$
($h00$)	[100][a]	1	2	0
	[010]	0	0	19.6
	[011][a]	0	0	19.6
($hh0$)	[110][a]	0.91	0.455	0.68
	[001][a]	0	0	19.6
	[$\bar{1}$10]	0	28.5	0
(hhh)	[111][a]	0.885	0	1.77
	[1$\bar{1}$0]	0	19.0	6.53
	[11$\bar{2}$][a]	0.008	17.3	9.4

[a]Directions used in the present investigation.

B. Small-q Approximation for S_{diff}: Asymmetry of Scattering Intensity

The antisymmetric contribution to S_{diff} given by Eq. (4c) results from an interference between the waves scattered from the long-range displacement field and the waves scattered from the defect itself and from its strongly distorted immediate neighborhood. Physically, the sum $\sum_n (1 - \cos\vec{h}\cdot\vec{t}^n)$ appearing in (4d) represents that number of atoms near the defect (or fraction thereof) which are displaced so strongly that they are totally out of phase with the reflected wave. For defects with large local displacements, like single interstitials, interstitial clusters, dislocation loops, etc., this term usually outweighs the contribution to η from the scattering amplitude $f_{\vec{h}}^{D}$ of the defect itself (see Table V for examples). For such defects η is always positive, so that the sign of the long-range displacements can be determined directly from the sign of S_{anti}. For defects which act as dilatation centers, such as interstitials, the scattering intensity increases at angles larger than the Bragg angle ($\vec{q}\cdot\vec{h} > 0$) and decreases at angles smaller than the Bragg angle ($\vec{q}\cdot\vec{h} < 0$). If the long-range displacement field is again expressed by the dipole force tensor, one obtains from Eq. (4c)

$$S_{\mathrm{anti}} = 2cf_{\vec{h}}^2 \eta_{\vec{h}} (h/q)(\tfrac{1}{3}\gamma^{(1)})^{1/2}(\mathrm{Tr}P_{ij}). \quad (9)$$

Strictly, Eq. (9) holds only for defects whose long-range displacement fields have cubic symmetry. For noncubic defects Eq. (4c) has to be averaged over all possible orientations. The average of the factor $\vec{h}\cdot\vec{t}(\vec{q})$ appearing in Eq. (4c) over all defect orientations alone always gives $(h/q)(\frac{1}{3}\gamma^{(1)})^{1/2}(\mathrm{Tr}P_{ij})$. Therefore Eq. (9) is a good approximation for defects whose long-range displacement field has deviations from cubic symmetry that are not too large (see Sec. IV C), if in this case only $\eta_{\vec{h}}$ is averaged over all orientations.

C. Diffuse Scattering for Larger Values of $\vec{q}$ and Strong Displacement Fields

If $q \geq 1/R_0$, where R_0 is that distance from the defect at which the displacements $t(R_0) \simeq 2\pi/h$,

the x rays image primarily the center of the defect and its highly distorted surrounding. If, as in a cluster, the contribution of the highly distorted surroundings dominates the scattering of the defect itself, the diffuse intensity can be approximated by considering the incoherent superposition of the Bragg intensities of locally strongly distorted regions [Stokes-Wilson (SW) approximation]. For the case of a defect with a displacement field

$$\vec{t}(\vec{R}) = (A_{cl}/R^2)\vec{\tau}(\vec{R}/R),$$

one obtains

$$S_{diff} = Cf_{\vec{h}}^2 \frac{h}{q^4 V_c} |A_{cl}| \phi_{SW}\left(\frac{\vec{q}\cdot\vec{h}}{qh}\right), \quad (10)$$

where ϕ_{SW} is an angular function which can only be evaluated for isotropic conditions. Trinkaus,[20] in addition, gets an oscillating factor. The region over which Eq. (10) is a good approximation[11] is given by

$$\frac{1}{(|A_{cl}|h)^{1/2}} \ll q \ll 4\frac{|A_{cl}|h}{V_{cl}}, \quad (11)$$

where the lower bound results from the condition that $\vec{t}\cdot\vec{h} \gg 1$ and the upper bound from the condition that the highly distorted volume around the cluster is larger than the volume V_{cl} of the cluster itself.

The most important differences between the scattering in the asymptotic region, given by Eq. (10), and the Huang scattering are (a) the $1/q^4$ decrease (instead of $1/q^2$), (b) the linear dependence on the defect strength which is proportional to A_{cl}, (c) the different angular variation of Eq. (5) and of ϕ_{SW}. Even for isotropic conditions ϕ_{SW} does not vanish for any direction of $\vec{q}$ with respect to $\vec{h}$. Therefore scattering intensity is expected all around the reciprocal-lattice points.

III. EXPERIMENTAL TECHNIQUE

A. Setup for X-Ray Measurements

Measurements of the intensity distribution around the reciprocal-lattice points must be made with single crystals and monochromatic radiation. For optimization of intensity and resolution, we used a focusing monochromator (Johannson type) and copper $K\alpha_1$ radiation. The quartz monochromator was specially developed[14] and adapted to a 6-KW rotating anode x-ray tube (Rigaku Denki). In order to take the intensity from the full breadth of the focal spot of the tube (0.05 mm with a 6° take-off angle), the angle subtended from the crystal to the focal spot should not be larger than the mosaic spread of the monochromating crystal. With a mosaic spread of 0.005° for quartz the large dimensions as indicated in Fig. 1 were necessary (distance from the focal spot to the monochromator of 500 mm, the radius of the focusing circle 1100 mm, and a quartz crystal of dimensions $80\times25\times0.5$ mm^3). Depending on the slits used (see Figs. 1 and 2) as many as 10^9 $K\alpha_1$ quanta/sec reached the sample. Behind the monochromator the plane aluminum sample which was sitting in a cryostat on the diffractometer could be adjusted in the focus of the monochromator [Fig. 1(c)] or in a "semifocusing" geometry, as shown in Figs. 1(a) and 1(b). The "semifocusing" condition (which would be focusing, if the sample were bent) can be achieved for transmission [Fig. 1(b)] as well as reflection [Fig. 1(a)] geometry by moving the diffractometer on a cross slide. All these movements could be made with the sample at 4 °K.

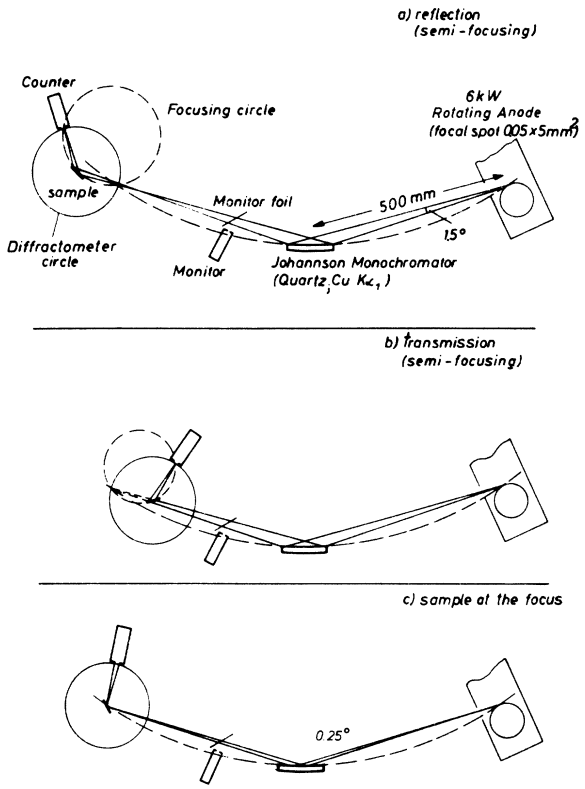

FIG. 1. Schematic view of the measuring system for the Huang scattering.

The advantages of the "semifocusing" system can be seen from Fig. 2 which shows the resolution in reciprocal space: The dimensions of the volume element of resolution are large tangential to the indicated equi-intensity lines of the diffuse scattering. Thus, it was possible to measure in radial direction in reciprocal space with a large divergence of the beam quite close to the reflection. For measurements vertical to the scattering vector this element was not favorable; and a

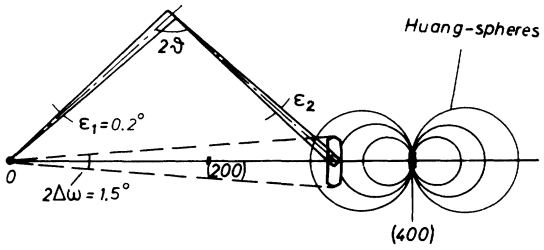

FIG. 2. Schematic view of the resolution volume element in reciprocal space. A cut in the $\vec{k}_0 - \vec{k}'$ plane is shown. The angles ϵ_1 and ϵ_2 are the angles under which the image of the focus and the detector, respectively, are seen from the sample position. $\Delta\omega$ is the divergence of the radiation coming from the monochromator. 2θ is the scattering angle which is equal for all the radiation scattered from the sample. In the direction perpendicular to the $\vec{k}_0 - \vec{k}'$ plane (i.e., in the direction perpendicular to the diffractometer plane) the divergence of the beam was limited by a solar collimator to about 2.0°.

smaller divergence was used as indicated in Fig. 1(c). All measurements were made with the sample in the focus as well as in the "semifocusing" arrangement. In this manner, both a small and large region of the sample were investigated. No systematic differences due to inhomogeneities of the samples were observed.

The movement of the resolution volume element in reciprocal space parallel to the scattering vector was achieved by a coupled 1:2 rotation of sample and counter. The movement in a direction perpendicular to the scattering vector was done with a fixed counter by rotating the sample. This rotation was achieved by a step motor which was started by a monitor counter. A small part of the incoming radiation was scattered to this monitor counter so as to obtain results independent of intensity variations of the x-ray tube and misalignments of the monochromator. Typical values were 100-sec measuring time and 0.25° steps in 2θ.

The diffracted radiation was counted with a proportional counter with a beryllium window. The energy resolution of the detector ($\approx 20\%$) gave a good intensity-to-background ratio and allowed the electric elimination of the harmonics of the Cu $K\alpha$ radiation. The background was less than 5 counts/min.

B. Conversion of Intensities to Absolute Units

In order to get the absolute cross sections from the observed scattering intensities it was necessary to know the primary beam intensity. Because of the high intensity in this experiment, no direct measurement was possible. The problems of absolute measurements have been discussed in Ref. 23. Here the method of a reference sample was used. The results were confirmed within 2% by an improved absorber technique.[14] The reference sample was polystyrene (C_8H_8) which was measured at a scattering angle 2θ of 100°. The experimental cross section given by Sparks and Borie[23] is 61.1 e.u. Using this cross section we obtain the scattering cross section of the sample by comparison of the intensities:

$$\frac{I}{I_R} = \frac{M_R \mu_R p \, d\sigma/d\Omega}{M \mu p_R (d\sigma/d\Omega)_R} , \tag{12}$$

where M is the molecular (or atomic) weight, μ the mass absorption coefficient, p the polarization factor, and the index R refers to the reference sample The values of M_R, μ_R, and $(d\sigma/d\Omega)_R$ for polystyrene were taken from Ref. 23. The polarization factor p depends on the scattering angles of the monochromator and the sample and was calculated for "mosaic crystals":

$$p = \frac{1 + \cos^2 2\theta \cos^2 2\theta_M}{1 + \cos^2 2\theta_M} , \tag{13}$$

where $2\theta_M = 26.70°$ is the Bragg angle of the monochromator. Formula (13) is a good approximation according to measurements of the polarization of a similar quartz monochromator.[24]

Formula (12) is correct for reflection from an infinitely thick sample in the symmetrical arrangement. For thin crystals and for transmission geometry, corrections are necessary. The correction factors $K = I_{\text{ideal}}/I_{\text{actual}}$ were calculated according to the International Tables[25] and are collected in Table III. For these calculations only the product μd is necessary (d is the thickness of the sample). This product can be determined directly from absorption measurements as $I/I_0 = e^{-\mu d}$.

To get information about the defect properties from the scattering cross section according to formula (1), one must know the atomic-structure factors $f_{\vec{k}}$ decreased by the thermal Debye-Waller factor (DWF), which was neglected in Eq. (1), at the measuring temperature of 4 °K. The DWF was calculated according to Ref. 26 using $\Theta_D = 398$ °K (see Table III).

In the actual evaluation of our Al data only the combination $(f_0 + \Delta f')^2/\mu$ enters. These values are listed in Table III. They have been taken from the powder data of Ref. 27 after correction for the DWF. The experimental error claimed in Ref. 27 is about 1% and the agreement of the f_0 value extracted from them with those calculated from Hartree-Fock theory is also better than 2%. However, the absorption factor $\mu = 50.4$ cm^2/g used in Ref. 27 for the calculation of f_0 from the experimental data is 4% higher than the value of 48.7 listed in the International Tables[25] and the value of 47.7 cm^2/g given in Ref. 28. In this latter

study only these lower values of μ are found to be consistent with the integrated intensity observed for rather perfect Al single crystals. On the other hand, a recent assessment[29] of the best data on μ confirmed the high value of 50.4 ± 0.5 cm^2/g. In view of this discrepancy we decided to use the combination $(f_0 + \Delta f')/\mu$ which has been measured directly in Ref. 27 and which, therefore, should not be affected so strongly by a possible systematic error in a separated determination of μ.

C. Samples

Al single-crystal slices with (110) orientation were cut from bulk material and planed by spark erosion. The material had a residual-resistance ratio between 300 and 1000 and a mosaic spread of up to 0.5°.

The first sample (Al I) was thinned from 600 to 95 μm in hot NaOH. The second (Al II) was brought to the final thickness of 85 μm by an electrolytic jet machining,[30] which allows a more controlled thinning of the sample. Sample Al I was thinned down over the whole area (21×17 mm^2) and was held only at one end. At sample Al II a thicker border was left and only the central part (18×15 mm^2) was thinned down. This eased the sample handling greatly. Although the connection between this central part and the thicker border was made much thinner than 85 μm and had been perforated at two sides, the lattice expansion due to radiation-induced defects caused more sample bending in this case than with sample Al I. Both samples were mounted on a holder such that the rotation axis of the diffractometer was parallel to the $[1\bar{1}0]$ axis in the surface of the sample. With this orientation the (220) Bragg reflection could be investigated in reflection geometry and the (200) and (400) reflection in transmission geometry with a symmetrical beam. The (222) reflection had to be measured in an asymmetrical reflection geometry (the sample was placed at the focus of the monochromator as focusing conditions were not easy to achieve); therefore, in these latter measurements the intensities and the resultant precision were considerably lower.

D. Irradiation Procedure and Sample Handling

The irradiations were performed in the low-temperature electronirradiation facility at Jülich described in detail elsewhere.[31] During the irradiation with 3-MeV electrons the samples were directly cooled by a stream of liquid helium. This technique allows irradiation of large specimen areas at 4.5 °K with high electron-beam densities (45 μA/cm^2 in our case). In all cases a resistivity sample made of the same material was irradiated along with the x-ray sample such that both samples received identical electron doses.

A water-cooled beam aperture defined the irradiated area of 14×14 mm^2. The electron beam was stopped in a Faraday cage used for the dose measurements.

After irradiation was terminated, the specimen was placed into a special transport cryostat (described in Ref. 32) in which it could be transferred into the x-ray cryostat. All this handling was done with the sample continuously immersed in liquid helium.

In the x-ray cryostat, the sample was cooled by pumping cold He gas through the sample chamber. Temperatures between 4 and 300 °K could be achieved by limiting the gas flow by a solenoid valve which was operated by temperature sensors (carbon resistors below 77 °K and thermistors above) located in the sample chamber.

Inside the cryostat the sample position could be adjusted by an x-y slide and by a tilting mechanism. In this manner the surface of the sample could be placed on the rotation axis of the goniometer, and the reciprocal-lattice vector of the reflection under investigation could be made parallel to the goniometer plane. More details of the cryostat are given in Ref. 14.

Two irradiation runs were performed, one with sample Al I and one with sample Al II. The electrical-resistivity changes introduced in these irradiations were $\Delta\rho_0 = 192$ and 120 nΩ cm for samples Al I and Al II, respectively.

After the irradiation, the diffuse scattering was measured near the (200), (400), (022), and (222) reflections in directions parallel and perpendicular to the scattering vector. These are the directions indicated in Table II. These measurements were repeated after different steps of an isochronal thermal-recovery program (annealing times of 20 min). All the x-ray measurements were made at 4.5 °K. The results of the measurements immediately after irradiation are reported in Sec. IV, whereas in Sec. V the results of the thermal-recovery experiments will be discussed.

IV. RESULTS FOR SINGLE INTERSTITIALS

Typical results for measurements directly after the irradiation are shown in Fig. 3. In order to compare the intensity in the radial [100] direction directly with that in the perpendicular [011] direction in reciprocal space, measurements are shown in which the sample was at the focus. In the semifocusing geometry the counting rates in the radial direction (2θ) were about five times higher. The Bragg peak intensity was $\approx 10^6$ counts/sec. The background intensity I_0 observed in the unirradiated sample is in good agreement with the estimated thermal diffuse scattering at 4.5 °K. It was the same, within experimental error, before irradiation and after complete annealing of the

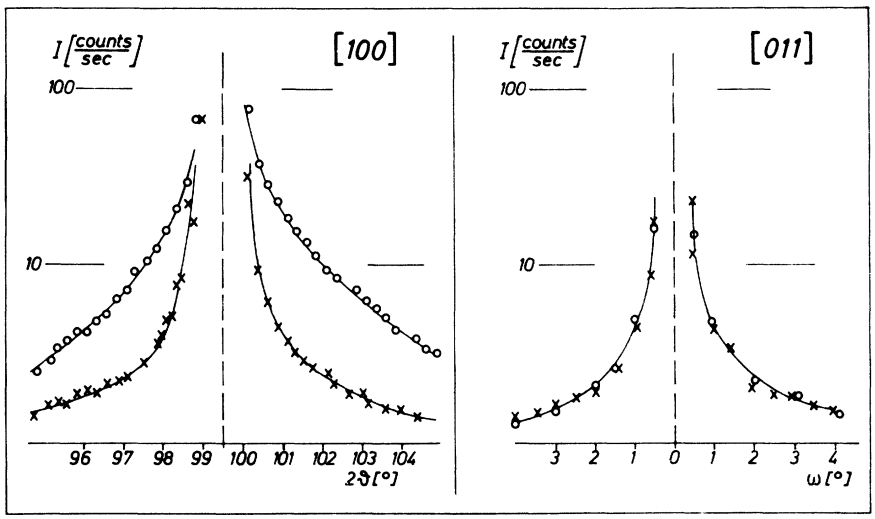

FIG. 3. Diffuse-scattering intensity measured at 4.5 °K for sample Al I near $\vec{h}=(400)$ in q directions along [100] and [011]. (×) are the data points before and (○) the data points after electron irradiation at 4.5 °K to $\Delta\rho_0 = 192$ nΩ cm.

defects at 300 °K. To obtain the net increase ΔI in diffuse intensity, this background was subtracted from the scattered intensity, i.e., $\Delta I = I - I_0$. From these differences the symmetric Huang intensity I_H was obtained by averaging the intensity changes at equal but opposite distances from the center of the Bragg peak, i.e., $I_H = \frac{1}{2}(\Delta I_{+q} + \Delta I_{-q})$. Similarly the antisymmetric part of the defect scattering intensity, I_{anti}, was obtained as $I_{\text{anti}} = \frac{1}{2}(\Delta I_{+q} - \Delta I_{-q})$.

In Fig. 4 the results for I_H in radial directions of $\vec{q}$ are plotted versus q/h for all the reflections investigated. The data points in this figure are mean values of two measurements in different scattering geometries (semifocusing and with the sample at the focus) and normalized to the values "at focus." If necessary, for the points very near to the reflections, resolution corrections have been calculated analytically, assuming isointensity surfaces to be spheres and the volume elements of resolution (as indicated in Fig. 2) to be disks for the focusing arrangements and lines for measuring "in focus." These corrections become negligible at distances larger than $q/h \simeq 0.03$ even for the lowest resolution used. In the case of the (222) reflection the angle-dependent part of the absorption correction has been done in order to demonstrate the $1/q^2$ dependence of the curve. From Fig. 4 one recognizes that for all reflections and for both samples the intensity I_H follows rather closely the $1/q^2$ dependence predicted by the theory. This demonstrates directly that in this case the $1/R^2$ part of the long-range displacement fields around the radiation-induced defects reaches quite close to the defect centers.

From the data in Fig. 4 the average ratio of the diffuse intensities observed for sample Al I and Al II can also be obtained. This ratio is 1.60 ± 0.03 for all the reflections shown and agrees very well with the ratio $\Delta\rho_0^{\text{I}}/\Delta\rho_0^{\text{II}} = 1.60$. This shows directly that the Huang intensity is proportional to the radiation-induced defect density [item (i) in Sec. II A]. This fact indicates that the defects which are responsible for the diffuse scattering are distributed statistically in the samples and that their density was low enough, such that the condition given by Eq. (3) is well fulfilled [e.g., using the Eqs. (14) and (15), $kt^{(1)}$ can be estimated to 0.01 for the (400) reflections]. Correlations in the interstitial arrangement which could build up at very high irradiation doses due to spontaneous recombination processes, apparently, are not important in the present experiments. This is also what one would expect from the magnitude of the defect densities employed which are well below the saturation density of $\Delta\rho_0^{\text{sat}} \sim 1000$ μΩ cm.[33] Both experiments[34] and theory[35] show that correlations in the defect pattern can build up at 4 °K only if the number of spontaneous recombinations which occurred in the sample during its irradiation history is very large compared to the number of defects which survive. To achieve this condition irradiation doses two orders of magnitude higher than those employed here are necessary. For sample Al I one can estimate that the number of defects eliminated by spontaneous recombinations was only 20% of the defects remaining. Thus, since the displacement process by the irradiating electrons is a statistical process and since rather few of the defects generated are eliminated by the spontaneous recombinations, the condition of a statistical distribution of the scattering centers is expected to be met rather well in our samples.

Since electron irradiation primarily produces single interstitials and single vacancies and since the scattering of an interstitial outweighs com-

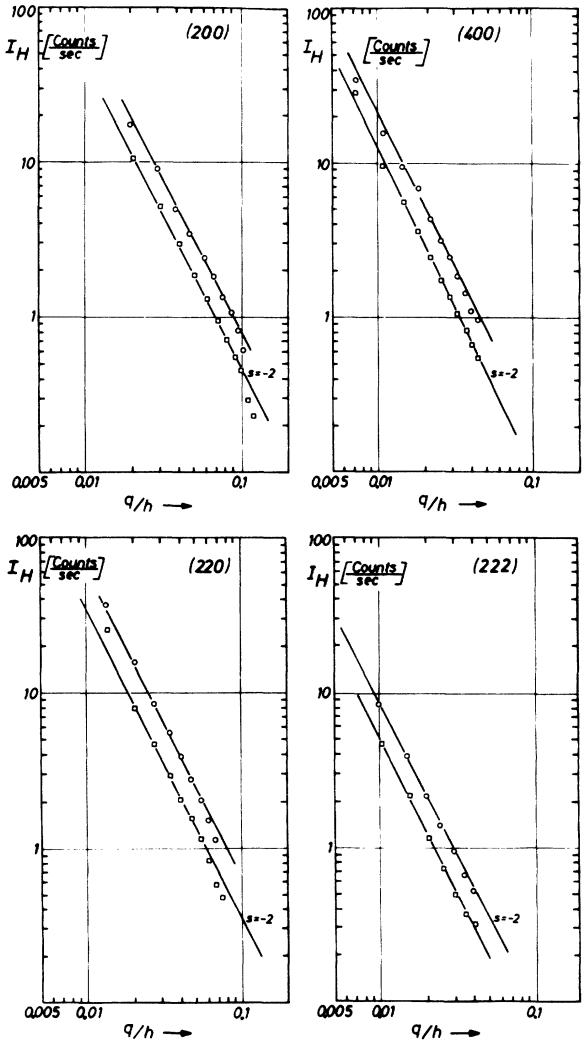

FIG. 4. Huang-scattering intensity I_H in radial direction in reciprocal space around the (200), (400), (220), and (222) reflections. (○): sample Al I ($\Delta\rho_0 = 192$ nΩ cm); (□): sample Al II ($\Delta\rho_0 = 120$ nΩ cm).

pletely the Huang-scattering cross section of a vacancy [see item (iv) in Sec. II A], the observed effects should give directly information about the long-range strain field of individual interstitial atoms. The fraction of defects generated by multiple displacement processes in Al during 3-MeV electron irradiation can be estimated to be less than 35%.[36] Furthermore, since no strong correlations in the distances between the interstitials produced in a multiple-displacement process are to be expected (see, e.g., the computer-simulation results given in Ref. 37), in this case also the scattering cross section per interstitial should deviate little from that of an isolated single interstitial. Furthermore, the vacancy generated close to each interstitial has rather little effect on the long-range displacement field of this interstitial. Recent model calculations[38] demonstrated that, for an interstitial once separated far enough from its vacancy to form a stable Frenkel pair, the displacements are practically equal to those around an isolated interstitial. In order to draw conclusions about the displacements around single interstitials from the observed changes in the diffuse scattering, one must further assume that the radiation-induced defect does not change the thermal diffuse background. This assumption is supported first by calculations of Eisenriegler[39] which show that for low defect densities the change in the inelastic x-ray scattering cross section is negligible compared to S_{Huang}. Second, from the magnitude of the measured change in the elastic constants in low-temperature irradiated Al,[8,45,46] the radiation-induced change in the thermal diffuse scattering near the Bragg peaks can be estimated to be less than 1% of the observed Huang-scattering intensity.

Having thus assured ourselves that the observed effects are related primarily to the displacement fields around single interstitials, we would like to discuss in the following sections the information which can be obtained from the experimental data about the symmetry and magnitude of this displacement field.

A. Symmetry of Long-Range Displacement Field

The most characteristic feature of the measurements after irradiation was that only in the radial and not in the perpendicular direction was an increase of the diffuse intensity observed around the (200), (400), and (220) reflections. From this it follows directly that the parameter $\pi^{(3)} \simeq 0$. Using the formulas tabulated in Table II from the experimental error, an upper limit of 1×10^{-3} can be estimated for the ratio $\pi^{(3)}/\pi^{(1)}$.

For the determination of the parameter $\pi^{(2)}$, the most sensitive $\vec{q}$ direction would be [110] at the

TABLE III. Parameters used for conversion to absolute intensities.

Reflection	Geometry θ (293 °K)	P	Absorption corr. K Al I	Al II	DWF (0 °K)	f^2/μ (g/cm^2)
(200)	Transmission 22.42°	0.775	1.46	1.41	0.97	1.46
(220)	Reflection 32.47°	0.635	1.008	1.011	0.941	1.11
(222)	Reflection (asym.) 41.17°	0.565	5.6[a]	5.6[a]	0.91	0.89
(400)	Transmission 49.50°	0.565	1.88	1.72	0.882	0.71

[a]Mean value—varies strongly with scattering angle because of highly asymmetric scattering geometry.

(220) reflection (see Table I). This measurement was not possible with the present sample geometry. The next-most-sensitive $\vec{q}$ direction is then $[11\bar{2}]$ at the (222) reflection. In this direction a small increase of $I^{[11\bar{2}]}/I^{[111]} \simeq (9 \pm 10)\%$ was observed. Due to the high asymmetry of the scattering geometry, however, the intensities are low and the absorption correction factor (see Table III) is large and strongly dependent of the scattering angle, so that the error associated with this intensity ratio is rather large. Using the formulas of Table II, one thus obtains $\pi^{(2)}/\pi^{(1)} = 6(^{+7}_{-6}) \times 10^{-3}$.

Comparison of these results with Table I shows that the strain field around the interstitial in Al has tetragonal or cubic symmetry. Since no model calculations for interstitials in Al are available, we compare our results in Table IV with the calculated dipole force tensors for interstitials in Cu.[1] This comparison suggests that the interstitials have the configuration H_O, but also the O and T configurations would be possible within the error limits of the present experiment. The configurations C, H_C, and H_T can be ruled out definitively. In Cu these configurations exhibit the greatest deviations from cubicity and it is not to be expected that the interstitials in Al behave very differently in this respect. The reason for this is that in the crowdion configuration the squeezed-in interstitial atom interacts primarily with its neighboring atoms in the close-packed ⟨110⟩ lattice row. Thus one expects that it generates forces on its surrounding which are much stronger in the ⟨110⟩ direction than in the directions perpendicular This always leads to a parameter $\pi^{(3)}$ which is not too different from the value $\pi^{(3)} = \frac{1}{2}\pi^{(1)}$ for a pure-⟨110⟩ force dipole.[41]

In contrast to this, the parameter $\pi^{(2)}$ calculated for the configuration H_O is two orders of magnitude smaller than that of the pure-⟨100⟩-force dipole given in Table IV. This difference is not surprising if one inspects the interaction of the H_O dumbbell atoms with their nearest-neighbor atoms in more detail. In H_O the atoms of the dumbbell are pressed towards a ring of four atoms and try to open this ring. This generates forces with large components perpendicular to the dumbbell axis, such that their first moment has almost cubic symmetry. In the configuration H_T the dumbbell atoms are pressed towards a ring of three close-packed atoms. This ring is more difficult to open, thus leading to a force distribution which shows larger deviation from cubic symmetry as H_O. But, as the parameter $\pi^{(3)}$ shows, this deviation is much smaller than that of the pure-⟨111⟩ dipole.

In summary, we can say that the diffuse-x-ray data definitively rule out the crowdion and H_C configurations and also the configuration H_T. The small finite value of $\pi^{(2)}/\pi^{(1)}$ observed points

TABLE IV. Experimental and theoretical values of the parameters $\pi^{(2)}/\pi^{(1)}$ and $\pi^{(3)}/\pi^{(1)}$ describing the deviation of the strain field from cubicity. The theoretical values for the various single-interstitial configurations pertain to the model calculations (Ref. 1) for Cu.

	Experimental values			Theoretical values for										
				Single force dipoles in direction			Single interstitials in configuration					Interstitial loops		
	Single interstitial	Di-interstitials	Interstitial clusters $n \approx 10$	⟨100⟩	⟨111⟩	⟨110⟩	O	T	H_O	H_T	H_C	C	On {111} planes with $\vec{b} = \frac{1}{3}a\langle 111\rangle$	On {111} planes with $\vec{b} = \frac{1}{2}a\langle 110\rangle$	On {110} planes with $\vec{b} = \frac{1}{2}a\langle 110\rangle$
$\pi^{(2)}/\pi^{(1)}$	$6(^{+7}_{-6}) \times 10^{-3}$	$9(\pm 3) \times 10^{-3}$	$0.02(^{+0.05}_{-0.02})$	1	0	$\frac{1}{4}$	0	0	0.002	0	0.007	0.012	0	0.012	0.012
$\pi^{(3)}/\pi^{(1)}$	$0(^{+1}_{-0}) \times 10^{-3}$	$0.012(\pm 0.002)$	$0.05(\pm 0.02)$	0	$\frac{2}{3}$	$\frac{1}{2}$	0	0	0	0.04	0.16	0.23	0.046	0.053	0.035

towards the configuration H_O, although the cubic configurations O and T are also compatible with our results within the experimental error. To distinguish between the H_O, O, and T configurations, diffuse-scattering data taken near the border of the Brillouin zone are necessary where primarily the structure factor of the interstitial itself enters into the scattering cross section.

B. Determination of Defect Strength and Absolute Concentration of Defects

For the further evaluation, the intensities shown in Fig. 4 have been converted into absolute cross sections using the procedure outlined in Sec. III B. From these cross sections the quantities $C\pi^{(1)}$ have been extracted using Eq. (5) and the atomic-scattering factors given in Table III and assuming $\pi^{(2)}$ and $\pi^{(3)} \simeq 0$ (see Table IV). For all reflections the quantities $C\pi^{(1)}$ agreed within 3%, demonstrating that the dependence on h^2 of the diffuse-scattering cross section [see item (ii) in Sec. II A] is also fulfilled rather well in our experiments. After division by $\Delta\rho_0$ (relative measure for the defect concentration $C = \Delta\rho_0/\rho_F$, where ρ_F is the resistivity per unit concentrations of interstitials plus vacancies), we obtain

$$\pi^{(1)}/\rho_F = (18.7 \pm 0.4) \times 10^5$$

and

$$(18.5 \pm 0.4) \times 10^5 \text{ eV}^2\,\Omega^{-1}\,\text{cm}^{-1}$$

for samples Al I and Al II, respectively. From the lattice-parameter and resisitivity measurements performed in Al irradiated under exactly the same conditions[42] and using Eq. (7), one further obtains

$$C(3\pi^{(1)})^{1/2}/\Delta\rho_0 = \mathrm{Tr}P_{ij}/\rho_F = (1.19 \pm 0.07) \times 10^5 \text{ eV}\,\Omega^{-1}\,\text{cm}^{-1}.$$

Combining these data, we arrive at

$$\mathrm{Tr}P_{ij} = 47 \pm 4 \text{ eV} \tag{14}$$

and

$$\rho_F = 3.9 \pm 0.6\ \mu\Omega\,\text{cm/at.\%} \tag{15}$$

for Al. The volume change per Frenkel defect is then $\Delta V = V_c 3(\Delta a/a) = 1.9 \pm 0.2$ atomic volumes [Eq. (7)]. The errors given for ρ_F and π also include the estimated systematic error connected with the atomic scattering amplitudes of Al (see Sec. III B). It should be mentioned that for this evaluation the only assumption which enters is that the contribution of the vacancies can be neglected in S_{Huang} (see Sec. II C) and in $\Delta a/a$. If the vacancies would contribute, e.g., -10% to the observed $\Delta a/a$, the ΔV and ρ_F values per Frenkel defect would decrease by about 10% and 20%, respectively.

C. Asymmetry of Diffuse Scattering

Measurements of the antisymmetric part $I_{\text{anti}} = \frac{1}{2}(\Delta I_{+q} - \Delta I_{-q})$ of the defect scattering intensity are shown in Fig. 5 for the (400) reflection. Similar data have also been obtained for the other reflections. The data points follow the $1/q$ dependence predicted by Eq. (9) only within a limited region. Close to the Bragg peak, I_{anti} becomes relatively small compared to I_{Huang} and the tails of the Bragg peak interfere too much. Further away from the Bragg peak, in addition to small counting rates, which reduce the accuracy, deviations are to be expected also because the approximations used to derive Eq. (4c) break down. Theoretically, for S_{anti} this should already happen at smaller q values than for S_{Huang}. This deviation could account for the more rapid decrease of I_{anti} at $q/h > 0.02$, where the Huang scattering still exhibits its $1/q^2$ behavior. Nevertheless, from the measurements of I_{anti} approximate values of the factor

$$\eta(\vec{h}) = \left| \sum_n (1 - \cos \vec{h} \cdot \vec{t}^{\,n}) - \mathrm{Re}\frac{f_{\vec{h}}^{D}}{f_{\vec{h}}} \right|$$

[see Eq. (9)] can be obtained using the information about C and $\pi^{(1)}$ derived from the Huang scattering. These values are listed in Table V where they are also compared with calculations for the different interstitial configurations H_O, O, and T.

As can be seen, there is rather good general agreement between the magnitudes of the experimental and theoretical values. This again confirms the conclusion drawn earlier that the diffuse scat-

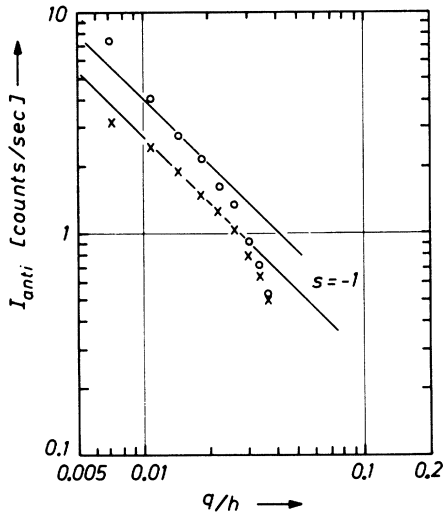

FIG. 5. Asymmetric part of the scattering intensity I_{anti}, measured at sample Al I along the [100] direction near the (400) reflection. (×): sample after irradiation; (○): sample annealed at 38 °K.

TABLE V. Experimental and theoretical values of the asymmetry parameter $\eta(\vec{h})$. The values for the different interstitial configurations H_O, O, and T have been calculated according to Eq. (4d) using the dumbbell length and nearest-neighbor displacements given in Ref. 1 for Cu. The contributions of the residual displacements have been estimated from continuum theory and the measured defect strength of Al. The numbers in parentheses give the values of $\mathrm{Re}(f_{\vec{h}}^{D}/f_{\vec{h}})$ calculated according to Eq. (2). For H_O an average has been taken over all possible orientations of the dumbbell. The experimental data on di-interstitials and interstitial loops refer to the sample annealed at 38 and 130 °K, respectively.

	Experiment			Theory (single interstitials)		
Reflection	Single interstitials	Di-interstitials	Interstitial loops	H_O	O	T
(200)	2.5 ± 30%	8 ± 40%	95 ± 60%	2.4 (−0.2)	1.9 (+1.0)	4.8 (−1.0)
(220)	5.5 ± 30%	21 ± 40%	180 ± 60%	6.6 (−1.4)	4.7 (+1.0)	5.1 (+1.0)
(400)	7.6 ± 30%	25 ± 40%	250 ± 60%	7.5 (+0.5)	7.6 (+1.0)	11.0 (+1.0)

tering is primarily due to the displacements around the radiation-induced interstitials.

The theoretical value for the tetrahedral configuration T for the (200) reflection seems to be somewhat outside the experimental errors. This tends to favor one of the other two configurations H_O or O.

V. RESULTS OF ANNEALING EXPERIMENTS: INTERSTITIAL CLUSTERING

In the course of the annealing experiments, very significant changes both in the absolute magnitude and the angular distribution of the diffuse scattering have been observed. Figure 6 gives a review of the results. For sample Al II, isochronal recovery curves are shown both of the electrical-resistivity change and of the diffuse intensity measured in $\vec{q}$ direction [100] and [011] around the (400) and (200) reflection. Each diffuse intensity data point represents the value of $q^2 I_{H,T}$ remaining after annealing at temperature T normalized to $q^2 I_{H,O\,°K}^{[100]}$. According to Eq. (5), I_H should be proportional to q^{-2}, so that a plot of $q^2 I_H$ should be insensitive to the detailed value of q at which I_H has been taken. The region where the $1/q^2$ dependence could be verified experimentally became rather small after annealing at higher temperatures (see Sec. V B). Therefore, the errors are correspondingly larger. For sample Al II the $I_{H,O\,°K}^{[011]}$ data observed at the (400) reflection right after the irradiation were not exactly zero as they were for sample Al I. This was due to a small flexure which occurred within the sample during the irradiation. These data points are therefore shown in parentheses in Fig. 6 and not included in the further evaluation.

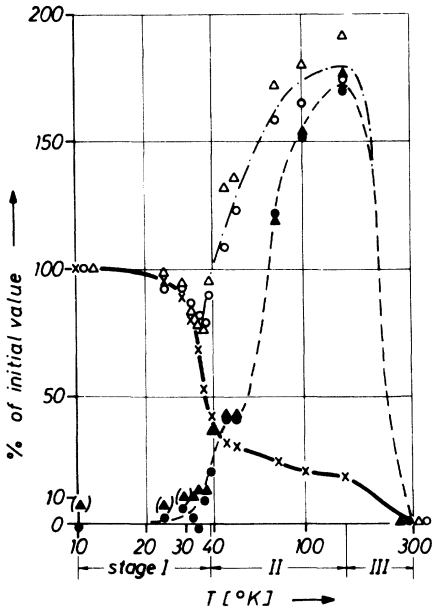

FIG. 6. Isochronal recovery of the electrical-resistivity change $\Delta\rho$ (points: ×) and of the diffuse intensity measured at the (200) reflection in q directions [100] (points: ○) and [011] (points: •) and at the (400) reflection in q directions [100] (points: △) and [011] (points: ▲) for sample Al II.

From Fig. 6 the following features can be recognized.

(i) Between 4 and 30 °K the diffuse intensity $I_H^{[100]}$ decreases in the same manner as the electrical resistivity. Since the electrical resistivity is a very good measure for the total defect density, this result shows that in this temperature range the decrease of the diffuse intensity is due to the decreasing number of interstitials only and that the scattering cross section per interstitial remains unchanged. This is consistent with the ideas that solely close Frenkel pairs recombine up to about 30 °K in Al. Also, the data for $I_H^{[011]}$ show that in this temperature range the structure of the interstitial remains tetragonal (or cubic).

(ii). In the final part of stage I (between 20% and 60% recovery in $\Delta\rho$ in Fig. 6, or $30 < T < 38$ °K), the diffuse intensity $I_H^{[100]}$ first drops off more slowly than $\Delta\rho$, turns over, and then increases. Also $I_H^{[011]}$ starts to increase. This shows that in this part of stage I, in addition to recombination, the interstitials cluster such that the increase in the scattering cross section per

interstitial (see Sec. IIA) outweighs and then overrides the decrease in the scattering intensity due to the loss of interstitials by recombination. This interstitial clustering process is a result of the free-interstitial migration occurring at the end of stage I and is responsible for the incomplete annealing in this stage. The increase in $I_H^{[011]}$ shows that the interstitial clusters formed in stage I no longer have a strain field with a pure tetragonal or cubic symmetry. A more detailed analysis of these clusters is given in Sec. V A.

(iii) In stage II (60% to 80% recovery in $\Delta\rho$ in Fig. 6, or $38 < T < 150$ °K) both $I_H^{[100]}$ and $I_H^{[011]}$ increase strongly. This shows that over this whole temperature range, where the resistivity decreases little, the interstitials more or less continuously grow into larger and larger clusters. A more detailed analysis of clusters present at the end of stage II is given in Sec. V B. Finally, in stage III (150–300 °K) both the resistivity and the diffuse scattering recover completely, showing that after this stage all the radiation-induced defects have recombined.

A. Identification of Di-Interstitials After Stage I

With sample Al I a more detailed study of the interstitial clusters present at the end of stage I and of stage II has been made. To this end after finishing the measurements directly after irradiation the sample was annealed at 38 and 130 °K. At 38 °K, judging from a detailed study of the electrical-resistivity annealing observed after similar irradiation doses, most of the free migrating interstitials have reacted, either with vacancies or with other interstitials. [In order to judge correctly at what temperature stage I is completed, one must have in mind that in Al right after stage I an additional small annealing stage (called stage II_1) is observed. In the annealing curves shown in Figs. 6 and 7, this stage was not resolved as a separate stage. However, detailed studies (see Ref. 43, Chap. I5) clearly revealed a separate stage II_1 after high-dose irradiation with electrons, α particles, and neutrons. After low doses, stage I usually extends to such high temperatures that no clear resolution of stage II_1 which has first-order character is possible.] After this annealing treatment the diffuse-x-ray intensity was studied at all the reflections and in all the directions as with the unannealed sample. Results of the measurements at the (400) reflection are shown in Figs. 7 and 8. Similar data have also been obtained for the other reflections. From these figures one recognizes the following characteristic differences with respect to the data shown in Figs. 3 and 4 for the single interstitials.

(a) The Huang-scattering intensity per defect has increased by about a factor of 2. This can be seen directly from Fig. 7; while after the 38 °K anneal, judging from the resistivity, the total number of defects has decreased about 50%, the diffuse intensity is about the same as before the annealing treatment.

According to the arguments given in Sec. IIA this fact suggests that after stage I the average cluster size is about 2, i.e., that the interstitials have survived primarily in the form of di-interstitials. In order to arrive at a more quantitative estimate of the interstitial cluster size, we compare the fractional changes, upon annealing, of both the Huang intensity and of the lattice-parameter change with the fractional recovery of the resistivity. On the one hand, from our experimental data we obtain

$$\frac{\pi^{(1)}|_{38\,^\circ\mathrm{K}}}{\pi^{(1)}|_{0\,^\circ\mathrm{K}}}\frac{\Delta\rho_0}{\Delta\rho_{38\,^\circ\mathrm{K}}} = 2.0 \pm 0.2 = \langle n\rangle_{\mathrm{av}}(1+\Delta)\frac{(1-y)^2}{1-x}\,, \tag{16a}$$

and from Ref. 42 we find

$$\frac{\Delta a/a|_{38\,^\circ\mathrm{K}}}{\Delta a/a|_{0\,^\circ\mathrm{K}}}\frac{\Delta\rho_0}{\Delta\rho_{38\,^\circ\mathrm{K}}} = 1.00 \pm 0.05 = \frac{1-y}{1-x}\,. \tag{16b}$$

On the other hand, from Eqs. (5) and (7) the theoretical expressions given above are derived. In these expressions $\langle n\rangle_{\mathrm{av}}$ is the mean number of interstitials per cluster, Δ is the relative mean square fluctuation of the defect number in the cluster so that $\langle n^2\rangle_{\mathrm{av}} = \langle n\rangle_{\mathrm{av}}^2(1+\Delta)$, and the quantities

$$y = 1 - V_{\mathrm{cl}}/\langle n\rangle_{\mathrm{av}} V_i$$

and

$$x = (\rho_i/\rho_F)(1 - \rho_{\mathrm{cl}}/\langle n\rangle_{\mathrm{av}}\rho_i)\,, \tag{17}$$

respectively, define relative deviation from the additivity of the contributions of the single interstitials (V_i, ρ_i) to the total volume change V_{cl} and the total resistivity ρ_{cl} of an interstitial cluster. When deriving the expressions (16a) and (16b), the assumption was made that x and y do not vary greatly with the cluster size. Otherwise the correction factors of Eq. (17) would have to be included in the averaging process.

Comparing the experimental results with the theoretical expressions in Eqs. (16a) and (16b) again leads to the conclusion that at 38 °K most of the interstitials are present as di-interstitials and that very little clusters with $n = 3$ or larger can be there. The argument is the following: First, we can exclude any sizable contribution to $\langle n\rangle_{\mathrm{av}}$ from single interstitials. Single interstitials can survive in stage I only by trapping reactions at impurities. From the purity of our sample

material and from annealing studies on Al of similar purity but much lower irradiation doses, we can estimate that only a negligible fraction (surely less than 5%) of interstitials could have been trapped as single entities. If, for the moment, we then take x and y both equal to zero, we find that the experimental average cluster size is equal to the smallest physically possible size, $n=2$. From this follows $\Delta \approx 0$ so that the distribution function has to be peaked strongly at $n=2$. Such behavior is also predicted by detailed kinetic analysis[7,43,44] of the interstitial clustering reactions in stage I. The physical reason for the supression of the clusters with $n>2$ is that the di-interstitials are an essential intermediate step for any larger interstitial cluster to form. So, by the time di-interstitials are abundant enough to be able to catch efficiently additional freely migrating interstitials during the annealing in stage I, the number of those has decreased so much that not many more larger clusters can be formed.

The conclusion that primarily di-interstitials are present at the end of stage I is also not changed if we allow for some reasonable nonadditivity in V_{cl} and ρ_{cl}. If, for instance, we take $x=0.1$ (since $\rho_i/\rho_F \approx 0.5$[8] this means already a 20% change in the resistivity per interstitial in the cluster), then from Eq. (16b) it follows that also y has to be about 0.1. Using this figure, Eq. (16a) yields a value of $\langle n \rangle_{av}$ which is still so close to $n=2$, that the fraction of clusters with $n \geq 3$ could be at most 10%.

(b) The intensities in the directions perpendicular to the reciprocal-lattice vectors no longer vanish. This shows that the di-interstitials formed in stage I no longer have pure tetragonal or cubic symmetry. The parameters $\pi^{(2)}/\pi^{(1)}$ and $\pi^{(3)}/\pi^{(1)}$ deduced from these data in the same manner as described in Sec. IV A are given in Table IV. Although the deviation from cubicity is still rather small, these data show that the two interstitials which form the di-interstitial must be aligned along one of the noncubic axes, e.g., along ⟨110⟩ or ⟨111⟩. Further one has to conclude that the strain

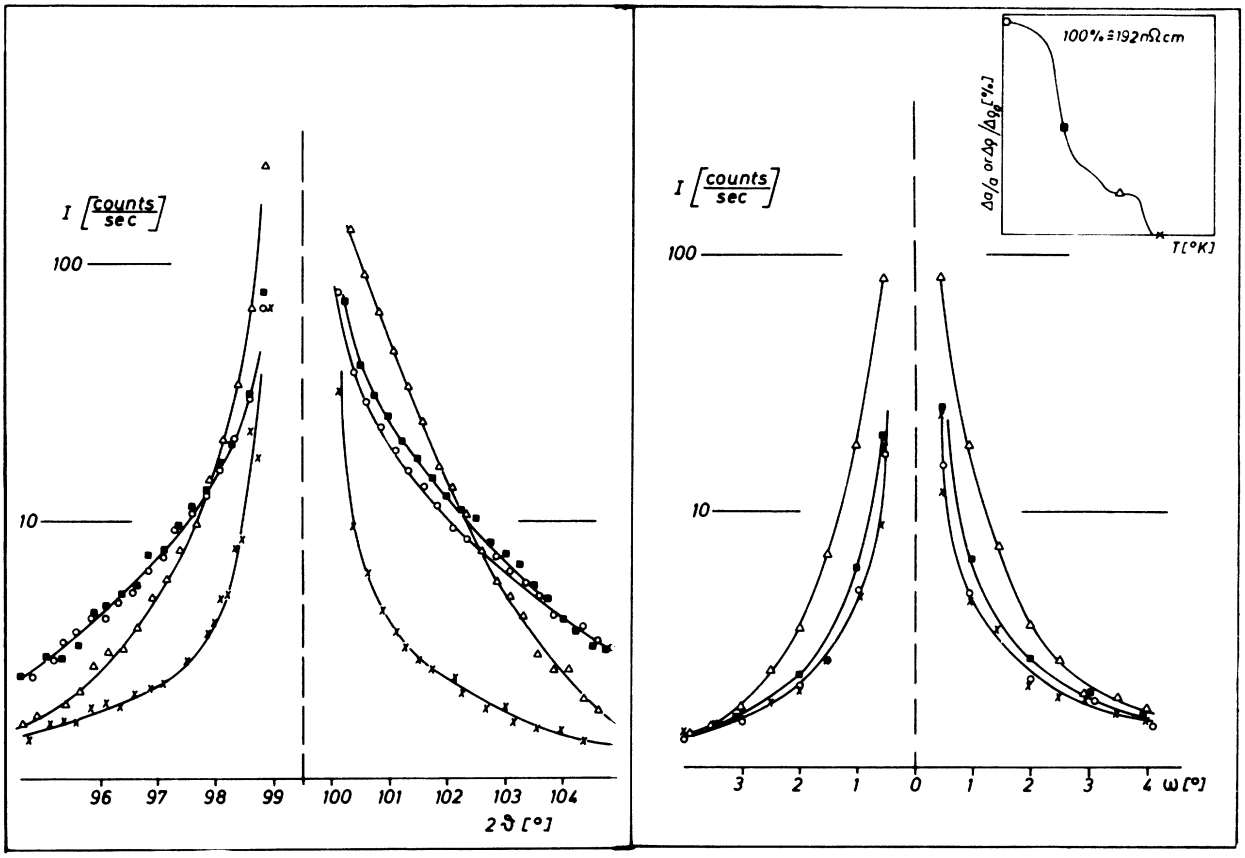

FIG. 7. Annealing behavior of the diffuse x-ray intensity measured at 4.5 °K for sample Al I near $\vec{h}=(400)$ in q direction parallel to [100] (left-hand figure) and along [011] (right-hand figure). (×) are the data points of the unirradiated sample. The annealing temperatures and percent recovery to which the other data points pertain are outlined in the insert.

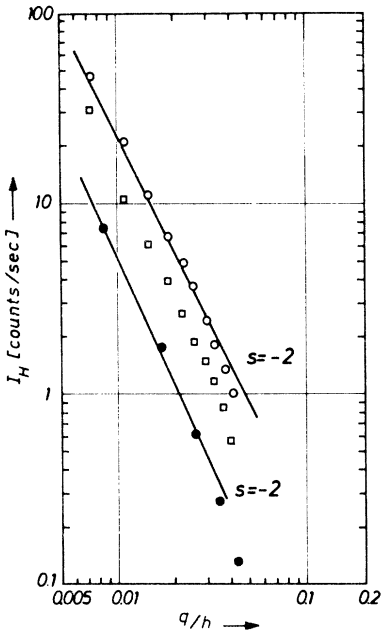

FIG. 8. Huang-scattering intensity I_H after annealing at 38 °K measured at the (400) reflection in q direction [100] (○: sample Al I; □: sample Al II) and in q direction [011] (●: sample Al I).

fields of the two interstitials forming the di-interstitial do not superimpose linearly. If this were the case, independent of the mutual arrangement of the two interstitials, the dipole-force tensor of the di-interstitials would be just the sum of the dipole-force tensors of the two single interstitials and the parameter $\pi^{(3)}$ would have to remain zero.

(c) Upon annealing to 38 °K the asymmetry of the intensity distribution around the Bragg peaks has increased. This is demonstrated by the increase in the quantities $\eta(\vec{h})$ given in Table V, which have been extracted from the measured values of I_{anti} in the same manner as described in Sec. IV C. In a continuum model, and neglecting $f_{\vec{h}}^{D}/f_{\vec{h}}$, one would expect [assuming that the displacements $\vec{t}^{n}$ are not too large and the cosine in (4d) can be expanded] $\eta \simeq \frac{1}{2}\sum_n (\vec{h}\cdot\vec{t})^2$. This would predict an increase in η for di-interstitials by a factor of 4, which is in approximate agreement with the experimental results. This finding confirms that after stage I the primary cluster size is $n \approx 2$. Since $\eta \propto \langle n^2 \rangle_{\text{av}}$, a larger contribution from clusters with $n \geq 3$ would give appreciably higher η values.

In conclusion, we can state that the diffuse-x-ray data taken at 38 °K indicate strongly that after stage I, interstitials are present primarily as di-interstitials. On the one hand, this rules out that di-interstitials are much more mobile than single interstitials, otherwise they would disappear along with the single interstitials. On the other hand, from the observed strong increase of the diffuse intensity with the annealing temperature above 38 °K one must conclude that these di-interstitials rapidly form larger clusters. The annealing stage II_1 mentioned before might thus be associated tentatively with the reactions of mobile di-interstitials with vacancies. The large internal-friction peak (called peak 2 in Refs. 45, 46, and 8) observed in irradiated Al at the end of stage I could then be interpreted as the thermally activated reorientation of di-interstitials in an external stress field. At temperatures just above stage II_1 (≈ 50 °K) the observed ratio

$$(I_{H,50\,^\circ\text{K}}^{[100]}/I_{H,0\,^\circ\text{K}}^{[100]})(\Delta\rho_0/\Delta\rho_{50\,^\circ\text{K}}) \approx 4.2,$$

indicating that the average cluster size is somewhat larger than 4. This suggests that few tri-interstitials are left above stage II_1, which in turn speaks against dissociation of the di-interstitials and in favor of a process which involves migration and mutual association of the di-interstitials.

B. Interstitial Clustering in Stage II

In Figs. 7 and 9 typical results of the measurements after annealing at 130 °K are shown. From a comparison with the results for di-interstitials (38 °K annealing) the following characteristic differences can be recognized.

(i) Close to the Bragg peak the intensity has further increased.

(ii) Only for rather small values of q/h is the $1/q^2$ dependence typical of the Huang scattering found. At larger distances from the Bragg peak the intensity drops off as $1/q^4$.

(iii) In the q direction perpendicular to the reciprocal-lattice vector, the intensity is of similar magnitude as in the radial direction.

In the following we first discuss the results close to the Bragg peak, i.e., in the region where the intensity decreases approximately as $1/q^2$. From these data the parameters $\pi^{(3)}$ and $\pi^{(2)}$ given in Table IV are deduced using the formulas given in Table II. The relatively high value of the parameter $\pi^{(3)}$ shows that the strain field of the interstitial clusters at 130 °K is highly anisotropic. Electron microscopic investigations of irradiated fcc metals (see Refs. 47 and 48 for reviews) suggest that the interstitials condense into dislocation loops. For such loops the parameters $\pi^{(1)}$ to $\pi^{(3)}$ can be calculated using the formulas given in Refs. 11 and 51. Results for $\pi^{(2)}/\pi^{(1)}$ and $\pi^{(3)}/\pi^{(1)}$ are given in Table IV. The experimental data agree best with the values calculated for sheared dislocation loops on $\{111\}$ planes; however, pure Frank loops on $\{111\}$ or $\{110\}$ planes would also be possible within our experimental errors.

In order to estimate the mean number $\langle n\rangle_{av}$ of interstitials per loop, we again extract from our data the ratio

$$\frac{\pi^{(1)}|_{130\,°K}}{\pi^{(1)}|_{0\,°K}}\,\frac{\Delta\rho_0}{\Delta\rho_{130\,°K}} = 8.0 \pm 2.0, \tag{18a}$$

and from the lattice-parameter measurement[42] the ratio

$$\frac{\Delta a/a|_{130\,°K}}{\Delta a/a|_{0\,°K}}\,\frac{\Delta\rho_0}{\Delta\rho_{130\,°K}} = 1.00 \pm 0.06. \tag{18b}$$

Combining these results with the theoretical expressions given in Eqs. (17a) and (17b) yields the following relationship:

$$\langle n\rangle_{av}(1+\Delta)(1-y) = 8 \pm 2. \tag{19}$$

To extract $\langle n\rangle_{av}$ from Eq. (19) requires information about the mean-square fluctuation Δ in the cluster size and about the parameter y describing the nonadditivity of the volume expansion per interstitial in the cluster. At the moment only upper and lower limits for these quantities can be established. An upper limit for y can be derived by recognizing that the volume change per interstitial on a (111) disk approaches just one atomic volume for very large clusters (if the contribution of the dislocation core to the volume change can be neglected). Thus for $V_i = 1.9$ atomic volumes [Eq. (14)] with the aid of Eqs. (7) and (17) an upper limit of $y \approx 0.47$ is obtained.

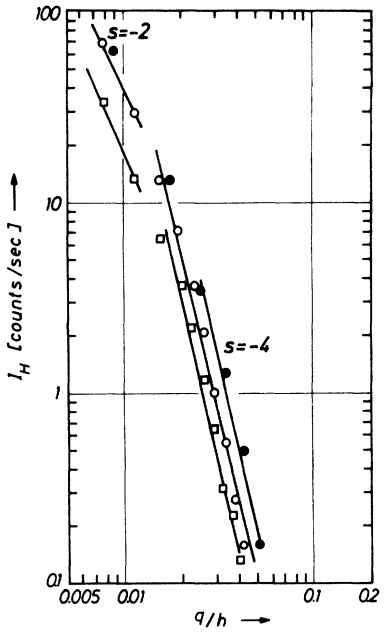

FIG. 9. Symmetrical part of the scattering intensity measured after annealing at 130 °K at the (400) reflection in the q direction [100] (○: Al I; □: Al II) and [011] (●: Al I).

The mean-square fluctuation Δ can be estimated assuming a distribution of the type $\exp[(R - R_{min})/R_0]$ for the cluster radii R which are cut off at some minimum radius R_{min}. Assuming that only clusters with $n \geq 7$ are stable at 130 °K [i.e., one interstitial surrounded by a hexagon of other interstitials on a (111) plane], we can calculate Δ as a function of the difference between average cluster size and minimum cluster size. This finally leads to an upper limit of $\langle n\rangle_{av} \approx 12$ with $\Delta \approx 0.25$ and $y \simeq 0.47$. Larger values of $\langle n\rangle_{av}$ would give greater values of Δ and would thus be incompatible with the experimental result given in Eq. (19). Similarly, a lower limit of $\langle n\rangle_{av}$ can be set up by assuming $y = 0$ and a minimum stable cluster size of $n \simeq 4$. This would then lead to $\langle n\rangle_{av} \simeq 6.5$ with $\Delta \simeq 0.25$. However, in view of the rather large values of the parameter y which are to be expected for dislocation loops, the assumption of $y \simeq 0$ is perhaps too unrealistic. For a more rigorous treatment of the volume change by interstitial loops the effect of the core of the dislocation must be regarded, too.[49,50] The volume change per interstitial in the loop is

$$\Delta V/NV_c = 1 - (\text{const})/N^{1/2}.$$

That shows that the value of $y = 0.47$ is too large. This formula is correct for very large dislocation loops, where the dislocation line can be approximated by a straight line and must be checked for our very small loops. Therefore, as the difference in $\langle n\rangle_{av}$ for the two limiting cases of y is not larger than the experimental error, we restrict our discussion to these simple limiting cases. Values of average cluster sizes near 10 seem to be most probable.

Completely independent information about the interstitial cluster size can be obtained from the asymmetry of the diffuse scattering. Although the measurements after 130 °K annealing showed a rather high asymmetry (see Fig. 7), only the data close to the Bragg peak, where also an approximate $1/q^2$ dependence of the Huang scattering was observed, could be used for an evaluation of η according to Eq. (4c). Taking $C_{c1}(\mathrm{Tr}P_{ij})_{c1}$ from the corresponding lattice-parameter measurements, the factors η given in Table V were thus obtained in the approximation of Eq. (9). According to Refs. 51 and 52 for loops of n interstitials, η can be estimated to

$$\eta_{loop} \simeq \tfrac{1}{2} n^{3/2} (h/\pi)^{3/2} V_c^{1/2}, \tag{20}$$

where an isotropic elastic medium has been assumed. The volume change per interstitial in the loop is 1 atomic volume. The scattering factor $f_{\vec{h}}^{D}$ of the loop can be neglected. The expression (20) already contains the averaging process over all equivalent loops and holds only if $qR_0 \ll 1$. Us-

ing Eq. (20), values of $\langle n^{3/2}\rangle_{av} = 47$, 53, and 44 are obtained from the η values at the (200), (220) and (400) reflections, respectively. From these figures, an average cluster size $\langle n\rangle_{av} \simeq 12$ is found, assuming again an exponential distribution of the loop radii which is cut off at $n \simeq 7$. Since the detailed form of the cluster-size distribution has less influence on $\langle n^{3/2}\rangle_{av}/\langle n\rangle_{av}^{3/2}$ than on $\langle n^2\rangle_{av}/\langle n\rangle_{av}^2$, a variation of the cutoff radius would affect the figure $\langle n\rangle_{av}$ calculated from $\langle n^{3/2}\rangle_{av}$ only a little. The good agreement between the values $\langle n^{3/2}\rangle_{av}$ extracted from the data at the different reflections and the agreement of $\langle n\rangle_{av} = 12$ with the value obtained independently from the Huang scattering gives strong evidence that the underlying physical picture is correct, i.e., that the interstitials at 130 °K have condensed into dislocation loops of average size $\langle n\rangle_{av} \simeq 10$, and that the volume change per interstitial has decreased in the loop to a value close to one atomic volume.

Assuming values of y near 0.47 for the interstitials in the cluster has the consequence that the parameter characterizing the nonadditivity of the contributions of the interstitials to the electrical resistivity must also be $x \simeq 0.5$. This follows directly from relation (18b) which expresses the fact that both the electrical-resistivity and the lattice-parameter change show identical annealing behavior. Using Eq. (19) and taking $\rho_i/\rho_F \simeq 0.5$,[8] we then have to conclude $\rho_{cl}/n\rho_i \simeq 0$. This would mean that a single interstitial by association at a dislocation loop would lose most of its electrical resistivity, which is perhaps not so unreasonable if the loops are large enough. In this case only the core of the dislocation, the length of which grows like $n^{1/2}$, contributes to the resistivity of the loop.

We now turn to a discussion of the measurement at larger distances q from the Bragg peak. There the $1/q^4$ behavior of the diffuse intensity predicted by the theory for strong displacement fields (Sec. II C) nicely fits the data (see Fig. 9). Also the predicted linearity in h is fulfilled within experimental error. However, in order to extract information from these measurements in the $1/q^4$ region, theoretical calculations of the angular function ϕ_{SW} entering in Eq. (10) are needed. Unfortunately this function is known only for isotropic defects, so that it cannot be applied directly to interpret the scattering from our highly anisotropic interstitial loops. For instance, the intensities observed in the axial q directions are about two to three times larger than in the radial direction, whereas the theory for isotropic defects predicts a ratio of 0.7. Nevertheless, comparing the average value of the intensity with the predictions of the theory for isotropic defects yields a value of $C_{cl}A_{cl}$ which is consistent with the value deduced from the lattice parameter change.

Recently, Larson and Schmatz[53] calculated numerically $S_{diff}(q)$ for dislocation loops on {111} planes in aluminum using the displacements predicted from linear elasticity theory for a disk of atoms. Although the results of these calculations did not show a large region with a well-defined q^{-4} dependence of S_{diff} (interference effects yield large oscillations of the calculated S_{diff} and strongly distort the decrease in the intensity in the region $qR \geq 1$; these oscillations are probably averaged out if a spectrum of loop sizes exist), they predicted appreciably higher intensities (up to factor of 5) in the perpendicular direction compared with the intensities in radial q directions. This result qualitatively agrees with the observation reported above. From a comparison of our data with these calculations another estimate for the loop sizes can be obtained. If we adjust the loop radius, R, which enters as a parameter in these calculations, such that in the calculated curves the transition from the q^{-2} region to the steeper decrease of S_{diff} occurs at the same q values as we observe experimentally, values of R between 5 and 7 Å are obtained. This gives numbers of interstitials per loop between $n \approx 10$ and 20, which is of the same order of magnitude as the values deduced from the Huang scattering and the asymmetry.

Summarizing the observations at 130 °K annealing temperature, we can state that the interstitials have condensed into highly anisotropic agglomerates, which are most probably dislocation loops on {111} planes and which contain, on the average, about ten interstitials per loop. Judging from the observed recovery behavior of S_{diff} between stages I and II (see Fig. 7), the transition from the di-interstitials to the dislocation loops takes place rather continuously with increasing temperature. Since the volume change per interstitial in the loop is considerably smaller than that of a single interstitial, from the constancy of the ratio of $(\Delta a/a)/\Delta\rho$ through stage II, one has to conclude that the contribution per interstitial to the electrical resistivity also decreases considerably in the loop. From the relative smallness of the observed total fractional resistivity recovery through stage II, one has further to conclude that rather few of the interstitials get lost during their transformation from di-interstitials into the loops. This largely excludes a growth mechanism of the loops based on dissociation of the smaller interstitial clusters into single entities and reassociation of the single interstitials to the larger loops. From the rather well-known reaction radii for interstitial-vacancy and interstitial-interstitial reactions,[44,54] one can judge that in this manner most of the interstitials would have to annihilate

at the vacancies and only few of them (at most something of the order of 10%) could finally survive in the form of clusters of $\langle n \rangle_{av} \approx 10$. This consideration points, therefore, to a growth of the larger loops by migration (or some kind of thermally activated drift in their mutual stress fields) and association of the smaller interstitial clusters into larger entities. The observation of several internal-friction maxima in the temperature range of stage II (peaks 3 to 5 in Refs. 45 and 46), which have been interpreted by the reorientation of interstitial clusters, gives further support to the idea of cluster mobility.

ACKNOWLEDGMENTS

We wish to thank Dr. T. O. Baldwin, Dr. P. H. Dederichs, Dr. E. Eisenriegler, H. G. Haubold, and Dr. W. Schmatz for many helpful discussions and U. Dedek and the operating team of the Van de Graaff for experimental assistance. We are very grateful to Dr. H. Trinkaus for making his papers available to us prior to publication. In addition, it is a pleasure to thank Dr. F. W. Young, Jr. for carefully reading the manuscript and for many helpful discussions.

*Present address: Solid State Division, Oak Ridge National Laboratory, Oak Ridge, Tenn. 37830.

[1]A. Seeger, E. Mann, and R. v. Jan, J. Phys. Chem. Solids **23**, 639 (1962).
[2]R. A. Johnson and E. Brown, Phys. Rev. **127**, 446 (1962).
[3]M. Doyama and R. M. J. Cotterill, in *Lattice Defects and Their Interactions*, edited by R. R. Hasiguti (Gordon and Breach, New York, 1967), p. 80.
[4]R. A. Johnson, Radiat. Eff. **2**, 1 (1969).
[5]W. Frank and A. Seeger, Radiat. Eff. **1**, 117 (1969).
[6]See, *Vacancies and Interstitials in Metals*, edited by A. Seeger, D. Schumacher, W. Schilling, and J. Diehl (North Holland, Amsterdam, 1970), p. 975.
[7]W. Schilling and K. Sonnenberg, J. Phys. F 2, 322 (1973).
[8]H. Wenzl, in Ref. 6, p. 386.
[9]L. S. Edelheit, J. C. North, J. G. Ring, J. S. Koehler, and F. W. Young, Jr., Phys. Rev. B 2, 2913 (1970).
[10]W. Schmatz, in Ref. 6, p. 589.
[11]P. H. Dederichs, J. Phys. F **2**, 471 (1973).
[12]H. Ekstein, Phys. Rev. **68**, 12 (1945).
[13]K. Huang, Proc. R. Soc. A **190**, 102 (1947).
[14]P. Ehrhart, Report of the Kernforschungsanlage, Jülich, Germany, Report No. Jül-810-FF, 1971 (unpublished).
[15]H. Lohstöter, H. Spalt, and H. Peisl, Phys. Rev. Lett. **29**, 224 (1972).
[16]T. O. Baldwin, F. A. Sherrill, and F. W. Young, Jr., J. Appl. Phys. **39**, 1541 (1968).
[17]J. E. Thomas, T. O. Baldwin, and P. H. Dederichs, Phys. Rev. B **3**, 1167 (1971).
[18]H. Spalt, Z. Angew. Phys. **29**, 269 (1970).
[19]H. Peisl, H. Spalt, and W. Waidelich, Phys. Status Solidi **23**, K75 (1967).
[20]H. Trinkaus, Z. Angew. Phys. **31**, 329 (1971).
[21]H. Trinkaus, Phys. Status Solidi B **51**, 307 (1972).
[22]M. A. Krivoglaz, *Theory of X-Ray and Thermal Neutron Scattering by Real Crystals* (Plenum, New York, 1969).
[23]C. J. Sparks and B. Borie, in *Local Atomic Arrangements Studied by X-Ray Diffraction*, Metallurgy Society Conference No. 36 (Gordon and Breach, New York, 1966).
[24]P. Suortti and T. Paakkari, J. Appl. Crystallogr. **1**, 121 (1968).
[25]*International Tables for X-Ray Crystallography* (Kynoch, Birmingham, England, 1962).
[26]A. Guinier, *X-Ray Diffraction* (Freeman, San Francisco, 1963).
[27]P. M. Raccah and V. E. Heinrich, Phys. Rev. **184**, 604 (1968).
[28]B. Nøst, B. C. Larson, and F. W. Young, Jr., Phys. Status Solidi A **11**, 269 (1972).
[29]G. D. Hughes, J. B. Woodhause, and I. A. Bucklow, J. Phys. D **1**, 695 (1968).
[30]P. Wombacher, J. Phys. E **5**, 243 (1972).
[31]J. Hemmerich, W. Sassin, and W. Schilling, Z. Angew. Phys. **29**, 1 (1970).
[32]J. Hemmerich, Report of the Kernforschungsanlage, Jülich, Germany, Report No. Jül-579-FN, 1969 (unpublished).
[33]G. Duesing, W. Sassin, W. Schilling, and H. Hemmerich, Cryst. Lattice Defects **1**, 55 (1969).
[34]K. Urban, Verh. Dtsch. Phys. Ges. **7**, 617 (1972).
[35]G. Lück and R. Sizmann, Phys. Status Solidi **14**, 507 (1966).
[36]W. Kesternich, Report of the Kernforschungsanlage, Jülich, Germany, Report No. Jül-851-FF, 1972, p. 93 (unpublished).
[37]C. Erginsoy, G. H. Vineyard, and A. Shimizu, Phys. Rev. **139**, A118 (1965).
[38]A. H. Scholz and Ch. Lehmann, Phys. Rev. B **6**, 813 (1973).
[39]E. Eisenriegler, Cryst. Lattice Defects **2**, 181 (1971).
[40]G. N. Kamm and G. A. Alers, J. Appl. Phys. **35**, 327 (1964).
[41]J. W. Flocken and J. R. Hardy, Phys. Rev. B **1**, 2472 (1970).
[42]H. Wagner, F. Dworschak, and W. Schilling, Phys. Rev. B **2**, 3856 (1970).
[43]W. Schilling, G. Burger, K. Isebeck, and H. Wenzl, in Ref. 6, p. 255.
[44]K. Schroeder, Radiat. Eff. **17**, 103 (1973).
[45]M. Rigganer, W. Schilling, J. Völkl, and H. Wenzl, Phys. Status Solidi **33**, 843 (1969).
[46]K. Ehrensperger, V. Fischer, J. Kerscher, and H. Wenzl, J. Phys. Chem. Solids **31**, 1835 (1970).
[47]M. Wilkens, in Ref. 6, p. 485.
[48]B. L. Eyre, J. Phys. F 3, 422 (1973).
[49]F. R. N. Nabarro, *Theory of Crystal Dislocations* (Clarendon, Oxford, England, 1967).
[50]J. Holder and A. V. Granato, Phys. Rev. **182**, 729 (1969).
[51]H. Trinkaus, Phys. Status Solidi B **54**, 209 (1972).
[52]P. H. Dederichs, Phys. Rev. B **1**, 1306 (1970).
[53]B. Larson and W. Schmatz (unpublished).
[54]D. E. Becker, F. Dworschak, and H. Wollenberger, Phys. Status Solidi **47**, 171 (1971).